Computational and Applied Mathematics (2026) 45:21
https://doi.org/10.1007/s40314-025-03406-5

An accurate and effective computational method to solve brain tumor problems: a Jacobian-free Newton Krylov method with an innovative preconditioning strategy II

Ece Hazal Korkmaz[1] · Samet Y. Kadioglu[1] · Ersin Ozugurlu[1]

Received: 26 March 2025 / Revised: 30 July 2025 / Accepted: 20 August 2025

Abstract
Brain glioma, a highly debilitating brain tumor, poses significant challenges for medical professionals and researchers globally due to its complex progression and invasive nature. Despite advancements in surgery, radiotherapy, and chemotherapy, glioblastoma multiform (GBM) remains notably resistant to treatment. Recent studies highlight the efficacy of the chemotherapy agent Temozolomide (TMZ) in enhancing survival rates, particularly when combined with radiotherapy. However, the optimal sequencing and combination of these treatments remain under investigation. Mathematical modeling has emerged as a powerful tool to simulate glioma behavior and optimize treatment strategies. These models incorporate biological principles, clinical data, and treatment parameters, using reaction-diffusion equations to replicate tumor growth dynamics. This paper explores the application of sophisticated mathematical and computational models to simulate the interplay between radiotherapy, chemotherapy, and glioma progression, aiming to develop optimized treatment strategies. By employing the Jacobian-free Newton Krylov (JFNK) method and an innovative physics-based preconditioning technique, we demonstrate computational accuracy and efficiency that improve treatment optimization. Our findings emphasize the potential of these models to enhance therapeutic outcomes for GBM patients.

Keywords Glioblastoma multiform (GBM) · Treatment strategies · JFNK method · Physics based preconditioner

Mathematics Subject Classification 35 · 65 · 92

1 Introduction

Brain glioma, an incapacitating form of brain tumor, persists in presenting substantial hurdles for medical professionals and researchers on a global scale. The complex progression of glioma and its invasive attributes necessitate the formulation of inventive and efficacious

✉ Samet Y. Kadioglu
kadioglusy@itu.edu.tr

[1] Department of Mathematical Engineering, Istanbul Technical University, 34667 Maslak, Istanbul, Turkey

Published online: 08 September 2025

treatment approaches. In the pursuit of effective treatments for glioma, surgery, radiotherapy, and chemotherapy have played central role in managing glioma progression Usher and Abercrombie (1981); Swanson et al. (2008); Rockne et al. (2010); Hormuth-II et al. (2022); Zhao et al. (2022); Kuznetsov and Kolobov (2023); Swanson et al. (2002); Perry (2012); Ansarizadeh et al. (2017); Liu and Liu (2017); Moreau et al. (2021). Despite the considerable advancements achieved in surgical and radio-chemotherapeutic methods, glioblastoma (GBM) continues to display significant resistance to treatment. In instances where surgical resection is impractical, radiation therapy (RT) emerges as the primary approach Barani and Larson (2015). The implementation of postoperative RT has also proven effective in improving survival rates for GBM patients Walker et al. (1976, 1980). In the past, chemotherapy was not preferred since the existing drug agents were unable to penetrate the tumor region due to the brain's low vascular permeability Powathil et al. (2007). A relatively recently developed chemotherapy agent called Temozolomide (TMZ) seems to penetrate the tumor region and has exhibited its effectiveness in enhancing survival outcomes for individuals with GBM Parney and Chang (2003); Stupp et al. (2005, 2009); Athanassiou et al. (2005). In a study Parney and Chang (2003), Parney et. al. extensively examined various pharmacological options and proposed that the overall survival of glioblastoma patients experiences a notable increase with the use of temozolomide, as opposed to alternatives such as procarbazine. Moreover, temozolomide demonstrated reduced toxicity and was better tolerated especially by elderly patients Parney and Chang (2003). In Stupp et al. (2005), Stupp *et. al.* conducted an assessment of radiotherapy concurrent with temozolomide across a cohort of 573 glioblastoma patients from 85 medical centers. They also concluded that temozolomide based chemotherapy led to prolonged survival with minimal associated toxicity. Chemotherapy can be administered in various regimens, either prior to (neo-adjuvant), simultaneously with (concurrent), or subsequent to a radiotherapy (adjuvant) Powathil et al. (2007); Barazzuol et al. (2010); Elazab et al. (2019); Bashkirtseva et al. (2021); Zade et al. (2022). Various clinical trials have been proposed with fractionation schedules Parney and Chang (2003); WANG et al. (2009); Powathil et al. (2013); Zade et al. (2022); Samadifam and Ghafourian (2023). Despite the resource-intensive and costly nature of clinical trials, we have to note that the findings are limited to small pools of patients Deisboeck (2009).

Mathematical models offer a potent tool to simulate and predict the behavior of brain gliomas under various treatment conditions. By integrating biological principles, clinical data, and treatment parameters into mathematical frameworks, these models incorporate reaction-diffusion equations to replicate tumor growth dynamics and optimize treatment strategies Tracqui et al. (1995); Swanson et al. (2003); Rockne et al. (2009); Powathil et al. (2007, 2013, 2015). Over the past two decades, the utilization of mathematical modeling has attracted considerable attention for studying the growth patterns and treatment responses Swanson et al. (2002, 2003); Powathil et al. (2007); Roniotis et al. (2010); Swanson et al. (2008); Rockne et al. (2009); Schuetz et al. (2014); Powathil et al. (2015); Mihalef et al. (2008); Tseng and Liu (2021); Khan et al. (2022); Zhao et al. (2022); Plaszczynski et al. (2023).

Tracqui et al. (1995) initially established a mathematical framework depicting the growth of gliomas, focusing on the interplay between proliferation and diffusion rates. They pioneered the modeling of glioma chemotherapy by representing the chemotherapy as a spatially uniform equation within a reaction-diffusion system. Examining the patients with anaplastic astrocytoma who received chemotherapy, the model's simulation aligned with clinical information obtained from CT scans. Similarly, Woodward et al. (1996) explored the nuances of diffusion and growth rates within gliomas. Extending this line of inquiry, Swanson et al. (2002, 2008) proposed a model that accounted for the brain's heterogeneity by differentiat-

ing between gray and white matter, incorporating space-dependent diffusion characteristics to better understand the effects of proliferation and diffusion within both tissue types. The slower diffusion rate in the gray matter region, which leads to prolonged drug exposure, was shown to enhance chemotherapy effectiveness. Radiation therapy, modeled within a reaction-diffusion framework by Swanson, was subsequently adapted by Rockne et al. (2009) to account for the effects of radiotherapy on cancer cell reduction. Similarly, Hathout et al. (2016) applied a reaction-diffusion equation to investigate the potential impact of surgical resection on glioblastoma. Exploring a range of resections and radiotherapy combinations, Moshtaghi-Kashanian et al. (2018) simulated glioblastoma growth under 100%, 105%, and 125% resections. Ghafourian et al. (2023) initiated a study on an integrated model for brain tumor diagnosis using MRI scans.

While the standard approach for GBM treatment involves combining radiation therapy (RT) and chemotherapy (CT), the early models have not used the simultaneous planning of these two modalities for GBM patients. Powathil et al. (2007) scrutinized the impacts of various radiation therapy timetables, including fractionated and hyperfractionated external beam radiotherapy, utilizing a generalized linear quadratic (LQ) model. Additionally, they analyzed outcomes related to combined treatment, integrating radiotherapy with a novel chemotherapy agent (Temozolomide). Their numerical results suggest that a sequence involving neo-adjuvant chemotherapy followed by radiotherapy and then adjuvant chemotherapy might offer a more advantageous approach, resulting in reduced toxicity, compared to the simultaneous administration of radiotherapy and chemotherapy, succeeded by adjuvant chemotherapy. Bashkirtseva et al. (2021) explored the impact of altering the sequence of delivering cytotoxic drugs and radiation in cancer treatment, comparing a sequential approach with a simultaneous chemo-radiation protocol. Using bifurcation theory, they illustrated that administering radiotherapy concurrently, after the chemotherapeutic regimen has induced significant tumor reduction, could be more relevant than the opposite approach, especially when bi-stability was observed. Consequently, their analysis suggests that appropriately arranging the timing and concurrency could offer potential advantages in the context of chemo-radiation for solid tumors. Nevertheless, the intricate task of maximizing the efficacy of radiotherapy and chemotherapy for optimal treatment results remains a challenging undertaking Kuznetsov and Kolobov (2023). The success of these therapeutic interventions is contingent upon diverse factors, including tumor size, location, and the individual responses of patients. Consequently, a critical imperative exists to formulate accurate and individualized strategies capable of customizing treatment protocols for each patient. Additionally, the effectiveness of the combined treatment models has been hindered by the ever existing computational demands preventing their practical application to tumors of realistic sizes. Recently, Zade et al. (2022) introduced a framework based on deep reinforcement learning (RL) to customize personalized chemo-radiotherapy (CRT) strategies, significantly improving both the algorithm's computational capabilities and the quality of the resulting regimens.

In this study, we aim to explore the mathematical and computational modeling of brain gliomas and their treatments. By developing advanced mathematical models, our objective is to simulate the complex interactions between radiotherapy, chemotherapy, and glioma progression. The objective is to devise optimized treatment strategies that minimize tumor growth and maximize patient outcomes. We utilize a validated simulated GBM to explore how tumors respond to different chemo-radiotherapy (CRT) approaches within the proliferation-invasion (PI) frameworks Powathil et al. (2007); Zade et al. (2022); Rockne et al. (2010). Furthermore, we examine the impact of fractionation and delivery timing on tumor control by combining chemotherapy, either adjuvantly or concurrently, with normal and hyperfractionated radiation treatment approaches. Certain model elements, including the initial tumor

profile and the staggered chemotherapy administration, are also refined in the treatment plan to yield the best survival outcomes.

General glioma progression with treatment strategies is often modeled by a reaction-diffusion type equation system. In literature, various numerical approaches have been developed to solve such systems. For instance, by converting the reaction-diffusion equation into an analogous integral equation, Wu et al. (2015) presented the variational iteration method (VIM) in 2015 to investigate this issue. One can avoid treating the time derivatives in the traditional sense of finite differences by using this technique. Nevertheless, the process uses what is known as the Picard iteration mechanism, which can be computationally inefficient. Further developments in this field include the work of Mach et al. (2017) , the finite-element nonlinear Galerkin method (FEM) in one spatial dimension, and its application to the chosen reaction-diffusion systems was studied. The element-free Galerkin method is another FEM technique that was used in 2018 by Dehghan and Narimani (2018) to model the impact of cancer cell invasion on the surrounding tissue. The computational aspects of these methods reveal significant challenges. Many approaches, including FEM, suffer from efficiency limitations due to excessive function evaluations or costly matrix operations.

While FEM maintains advantages in geometric flexibility, its computational expense typically exceeds that of finite volume or finite difference methods, while still struggling with stability in discontinuous systems. Recent advances have attempted to overcome these limitations. In 2020, Damm et al. (2020) solved the reaction-diffusion type model in multi-dimensional settings using a collocation meshless method known as the radial basis function-generated finite difference (RBF-FD) scheme. After approximating the time variable using a first-order semi-implicit scheme, they used the bi-conjugate gradient stabilized (BiCGSTAB) iterative method with a zero-fill incomplete lower-upper (ILU) preconditioner to solve the resultant linear system of algebraic equations. A disadvantage of this strategy is that, even if it is not comprehensive, it requires a costly LU decomposition, not to mention the Conjugate Gradient (CG) method's positive-definite requirement. Kapoor and Joshi (2021) conducted another investigation in 2021. They discretized the spatial partial derivatives in 1D and 2D reaction-diffusion systems using a modified cubic uniform algebraic hyperbolic tension B-spline differential quadrature technique. They solved the resultant ordinary differential equation (ODE) using a strong stability preserving Runge–Kutta (SSP-RK4) time scheme. Due to the high number of function evaluations in the cubic spline technique and the stability constraints imposed by the explicit SSP-RK4 method, this strategy has the potential to be costly to implement. There are successful high-order explicit methods recently studied for solving reaction-diffusion systems. Kovács et al. (2024) and Khayrullaev et al. (2025) have developed effective techniques that preserve dynamical consistency. These methods improve stability and accuracy compared to traditional explicit schemes, making them well-suited for handling the complex nonlinearities often present in such problems.

In this context, our computational methodology revolves around the utilization of the Jacobian-free Newton Krylov (JFNK) method, eliminating the need for constructing, storing, and inverting the Jacobian matrix. The JFNK method's implementation involves iteratively solving a linear system arising from the correction step. This linear system is addressed through a Krylov subspace method, specifically employing the Generalized Minimal RESidual (GMRES) iterative procedure Knoll and Keyes (2004); Saad (2003). The JFNK method, combined with GMRES technology, is effectively utilized to solve boundary or initial value problems arising from various applications, including compressible and incompressible fluid dynamics, heat transfer engineering, thermal hydraulics, neutronics, solid mechanics, astrophysical studies, and industrial optimization problems Knoll and Keyes (2004); Zhang et al. (2019); Kothari et al. (2023); Damm et al. (2023). In order to speed up convergence, every iter-

ative procedure usually requires a preconditioning phase. Based on the fundamental physics of the issue, we present a very effective preconditioning method that is similar to those described in Kadioglu and Knoll (2013); Kadioglu et al. (2011); Park et al. (2009); Kadioglu (2017, ?). Such a technique is frequently referred to as physical preconditioning or physics-based preconditioning in the literature. This preconditioning strategy's main benefit is its capacity to apply the process selectively rather than uniformly across the system, focusing on the parts of the model that cause stiffness or delayed convergence. The numerical results in Sect. 4 show how well the suggested preconditioner performs, confirming its ability to increase computational efficiency and showing notable decreases in the number of GMRES and Newton iterations. Section 4 also includes a detailed performance analysis comparing the newly proposed preconditioner with existing state-of-the-art preconditioning techniques, such as the Incomplete Lower-Upper (ILU) factorization methods.

The structure of this manuscript is as follows: Sect. 2 presents the governing equations, while Sect. 3 describes the JFNK method and introduces the novel physics-based preconditioning approach. Section 4 focuses on the numerical results, presenting the results of numerous tumor treatment strategies, validating the convergence of the numerical scheme, and illustrating the effectiveness of the preconditioning technique. Finally, Sect. 5 provides concluding remarks and discusses possible avenues for further study.

2 Governing equations

Based on the proliferation-invasion model, also known as the Fisher-Kolmogorov equation in the literature, the governing equations describe the invasion of glioma cells as a reaction-diffusion process and include the effects of radiation and chemotherapy Tracqui et al. (1995); Swanson et al. (2002); Powathil et al. (2007, 2013, 2015):

$$\begin{aligned}\frac{\partial c(x,y,t)}{\partial t} &= \frac{\partial}{\partial x}\left(D(x,y)\frac{\partial c(x,y,t)}{\partial x}\right)\\ &+\frac{\partial}{\partial y}\left(D(x,y)\frac{\partial c(x,y,t)}{\partial y}\right)+\rho c(x,y,t)\left(1-\frac{c(x,y,t)}{\kappa}\right)\\ &-R(\vec{x},t,Dose)\,c(x,y,t)\left(1-\frac{c(x,y,t)}{\kappa}\right)-G(c,t),\end{aligned} \tag{1}$$

where $c(x, y, t)$ is the tumor concentration of glioma cells (or the tumor cell density) at spatial locations x, y and time t, κ is called the carrying capacity that is the maximum number of tumor cells that can fit in a cubic millimeter of tissue. Once the tumor cell density, c, reaches the carrying capacity ($c = \kappa$) at a particular spatial location, the tumor cells are space restricted and therefore do not proliferate. ρ is the net proliferation rate that corresponds to a volume doubling time of 2 months for the exponential growth model and it is typically set to be $\rho = 0.012\,\text{day}^{-1}$. The diffusion coefficient, $D(x, y)\ cm^2\ day^{-1}$, that may vary from patient to patient Shim et al. (2005) is given by

$$D(x,y) = \begin{cases} 0.0065 & \text{if } 0 \le d \le 17.5 \text{ (white region)} \\ 0.0013 & \text{otherwise (gray region)}, \end{cases} \tag{2}$$

where $d = \sqrt{(x-x_0)^2+(y-y_0)^2}$ and $(x_0, y_0) = (4.0, 4.0)$ is the center of the two-dimensional computational domain $A = [0, 8] \times [0, 8]$.

Here, the radiotherapy coefficient term is defined as

$$R(\vec{x}, t, Dose) = R_{\text{eff}} R_{\text{timer}}(t), \tag{3}$$

where

$$R_{\text{eff}} = 1.0 - e^{-\alpha\left(Dose(\vec{x},t) + \frac{(Dose(\vec{x},t))^2}{\alpha/\beta}\right)}, \tag{4}$$

where α $(1/\text{Gy})$ is the sensitivity parameter that typically depends on patients. The larger the α is, the more sensitive the patients are to radiation therapy. Together with the other radio-biological parameter β $(1/\text{Gy}^2)$, the so-called sensitivity ratio α/β is usually taken to be a constant value of 10 Gy Rockne et al. (2010).

The remaining parameters in Eqns. (3) and (4) are as follows: $Dose(\vec{x}, t)$ denotes the radiation dose, and $R_{\text{timer}}(t)$ is the radiation timer function,

$$R_{\text{timer}}(t) = \begin{cases} 1 & \text{if } t \in \text{Therapy} \\ 0 & \text{if } t \notin \text{Therapy.} \end{cases} \tag{5}$$

The chemotherapy term is described as either based on the exponential decay

$$G(c, t) = G_{\text{timer}}(t)\, k\, c(x, y, t), \tag{6}$$

or based on the logistic decay

$$G(c, t) = G_{\text{timer}}(t)\, k\, c(x, y, t) \left(1 - \frac{c(x, y, t)}{\kappa}\right), \tag{7}$$

where k represents the average lethal rate of temozolomide and often taken to be a constant, and the chemotherapy timer function is given by

$$G_{\text{timer}}(t) = \begin{cases} 1 & \text{if } t \in \text{Therapy} \\ 0 & \text{if } t \notin \text{Therapy.} \end{cases} \tag{8}$$

More details about the radio and chemo therapy time scheduler functions will be presented in Sects. 4.1 and 4.2.

In this study, we use zero-flux boundary conditions along the all edges of the computational domain,

$$c_x(0.0, y, t) = c_x(8.0, y, t) = c_y(x, 0.0, t) = c_y(x, 8.0, t) = 0.0. \tag{9}$$

The initial tumor concentration can be defined in two alternative ways. One is based on the two dimensional Gaussian distribution centered at (x_0, y_0),

$$c(x, y, 0) = g(x, y) = c_{\max} e^{-\frac{d^2}{\epsilon}}, \tag{10}$$

and the other is based on the hyperbolic tangent function

$$c(x, y, 0) = g(x, y) = \frac{1}{2} c_{\max} \left(\tanh\left(\frac{\varphi}{\lambda}\right) + 1\right), \tag{11}$$

where $c_{\max}$ denotes the maximum value of tumor concentration that is typically equal to the carrying capacity, and $\varphi = r - d$ with r being the radius of the initial tumor region and d denoting the distance function described right after Eqn. (2). Here ϵ and λ are pre-set parameters that help to adjust the thickness of the regions where the tumor concentration jumps from zero to its maximum value. Through our numerical experiments, we came up with suitable values for ϵ and λ as $\epsilon = 0.1$ and $\lambda = 0.001$.

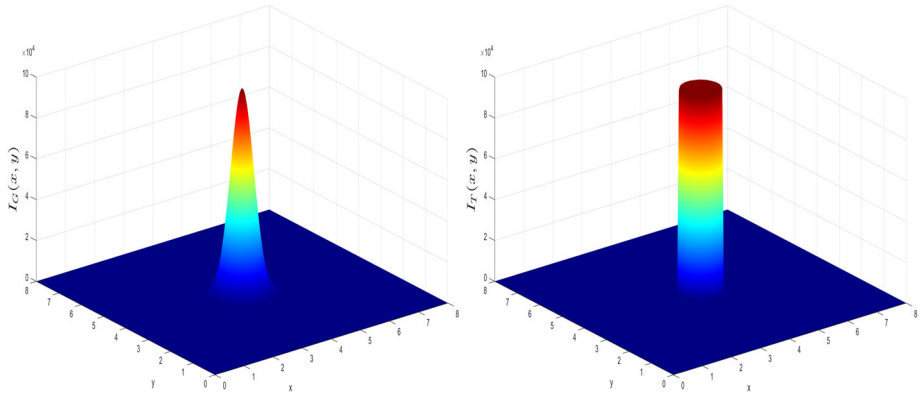

Fig. 1 The initial tumor concentration based on Left: the Gaussian profile, Right: the tanh profile

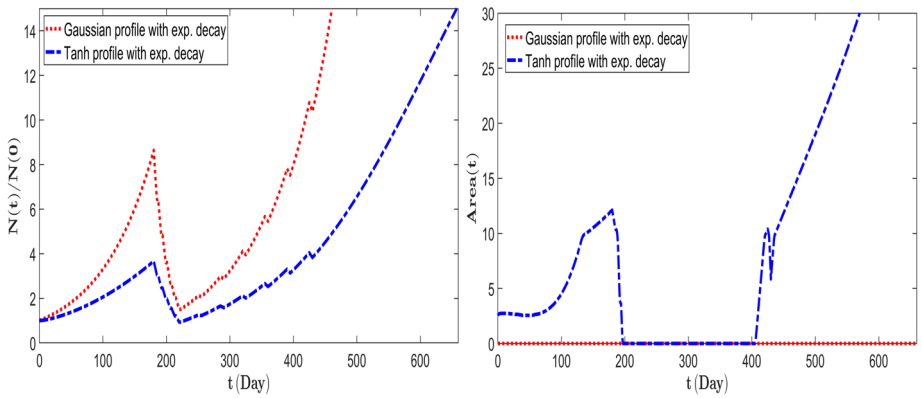

Fig. 2 Left: The normalized total number of tumor cells and Right: The simulated tumor areas based on Eqns. (10) and (11)

Figure 1 illustrates the initial tumor concentration profiles derived from Eqns. (10) and (11).

Figure 2 presents the outcomes of test simulations employing the conventional concurrent radio-chemotherapy treatment model, incorporating exponential decay terms for chemotherapy. In Fig. 2, numerical results corresponding to the initial Gaussian and hyperbolic tangent profiles, as defined by Eqns. (10) and (11), are compared. The left panel displays a comparison of the normalized total tumor cell count, while the right panel contrasts the detectable tumor regions. The total tumor cell count across the computational domain is calculated by

$$N(t) = \iint_A c(x, y, t)dxdy. \tag{12}$$

The time-dependent tumor area, $Area(t)$, is calculated based on specific detection criteria. In this study, it was observed that the initial tumor concentration profile derived from the hyperbolic tangent function yields more realistic estimates of tumor cell numbers and tumor areas. Conversely, the Gaussian initial profile overestimates the total tumor cell count and fails to accurately represent tumor areas. For instance, when a detection threshold of 400 cells per mm^2 (or 40000 cells per cm^2), consistent with CT scan criteria, is applied, the computed

cell density from the Gaussian initial profile consistently remains below this threshold. Due to the inability of the Gaussian initial profile setting to detect tumor cells, the corresponding area value is assigned as zero (represented by the red line in the right panel of Fig. 2). This discrepancy arises because equation (10) features a sharp gradient, which leads to the rapid collapse of the initial profile and excessive spreading. Another reason the Gaussian profile is unsuitable for computationally initiating gliomas is that human tissue can only sustain a limited number of tumor cells and cannot accommodate excessively high concentrations.

3 Numerical method

The well-known Crank–Nicolson approach LeVeque (1998); Thomas (1998) serves as the foundation for the numerical discretization used in this work. The Crank-Nicolson method is a second-order accurate scheme in both space and time. It utilizes the time average of the flux and other source terms, along with centered spatial discretizations. While the Crank-Nicolson scheme offers good accuracy for many applications, one could alternatively employ methods such as the second-order Backward Difference Formula (BDF2) or other advanced temporal discretization approaches, depending on the specific requirements of the problem. We note that the BDF2 method has a larger stability region for stiff problems than the Crank-Nicolson scheme, but it introduces numerical dissipation by damping high-frequency components, which can lead to smearing. Additionally, the Crank-Nicolson method has less truncation error than the BDF2 and maintains sharp gradients in the solution Thomas (1998).

The discretization of the governing equation in Eqn. (1) in conjunction with these guidelines results in

$$\frac{c_{i,j}^{n+1}-c_{i,j}^{n}}{\Delta t}-\left[\frac{\partial}{\partial x}\left(D\frac{\partial c}{\partial x}\right)\right]_{i,j}^{n+\frac{1}{2}}-\left[\frac{\partial}{\partial y}\left(D\frac{\partial c}{\partial y}\right)\right]_{i,j}^{n+\frac{1}{2}}-\left[\rho c\left(1-\frac{c}{\kappa}\right)\right]_{i,j}^{n+\frac{1}{2}}+\left[Rc\left(1-\frac{c}{\kappa}\right)\right]_{i,j}^{n+\frac{1}{2}}+G_{i,j}^{n+\frac{1}{2}}\approx 0, \tag{13}$$

where the terms ρ, D, R, and G are described in Sect. 2. Here the time averaged quantities represent $[-]^{n+\frac{1}{2}}=[(-)^{n+1}+(-)^{n}]/2$ and the spatial derivative terms are defined as

$$\frac{\partial}{\partial x}\left(D\frac{\partial c}{\partial x}\right)_{i,j}=\frac{D_{i+\frac{1}{2},j}c_{x\,i+\frac{1}{2},j}-D_{i-\frac{1}{2},j}c_{x\,i-\frac{1}{2},j}}{\Delta x},\quad D_{i+\frac{1}{2},j}=\frac{D_{i+1,j}+D_{i,j}}{2},$$

$$c_{x\,i+\frac{1}{2},j}=\frac{c_{i+1,j}-c_{i,j}}{\Delta x},\quad D_{i-\frac{1}{2},j}=\frac{D_{i,j}+D_{i-1,j}}{2},\quad c_{x\,i-\frac{1}{2},j}=\frac{c_{i,j}-c_{i-1,j}}{\Delta x}, \tag{14}$$

$$\frac{\partial}{\partial y}\left(D\frac{\partial c}{\partial y}\right)_{i,j}=\frac{D_{i,j+\frac{1}{2}}c_{y\,i,j+\frac{1}{2}}-D_{i,j-\frac{1}{2}}c_{y\,i,j-\frac{1}{2}}}{\Delta y},\quad D_{i,j+\frac{1}{2}}=\frac{D_{i,j+1}+D_{i,j}}{2},$$

$$c_{y\,i,j+\frac{1}{2}}=\frac{c_{i,j+1}-c_{i,j}}{\Delta y},\quad D_{i,j-\frac{1}{2}}=\frac{D_{i,j}+D_{i,j-1}}{2},\quad c_{y\,i,j-\frac{1}{2}}=\frac{c_{i,j}-c_{i,j-1}}{\Delta y}. \tag{15}$$

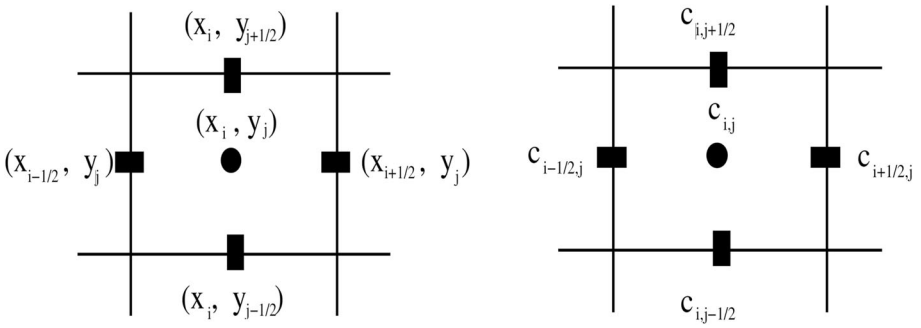

Fig. 3 A staggered grid cell (left) and a solution representation (right)

In the discrete equation (13), $c^n_{i,j}$ represents an approximation to the true solution at the grid location $(x_i,\ y_j)$ and time t_n, $c^n_{i,j} \approx c(x_i,\ y_j,\ t_n) = c(i\Delta x,\ j\Delta y,\ n\Delta t)$, where $\Delta x = x_{i+\frac{1}{2}} - x_{i-\frac{1}{2}}$ and $\Delta y = y_{j+\frac{1}{2}} - y_{j-\frac{1}{2}}$ are the size of the $(i,\ j)^{th}$ cell in x and y directions, $(x_i,\ y_j)$ represents the center of the $(i,\ j)^{th}$ cell, and $(x_{i\pm\frac{1}{2}},\ y_{j\pm\frac{1}{2}})$ denote the left, right, top, and bottom edges of the $(i,\ j)^{th}$ cell (refer to Fig. 3). The spatial domain $[0,\ 8.0] \times [0,\ 8.0]$ is divided into M_x and M_y sections in x and y directions. We use uniform grids in this study implying that $(\Delta x_i,\ \Delta y_j) = (\Delta x\ ,\ \Delta y) = (\frac{8.0}{M_x},\ \frac{8.0}{M_y})$ where $i = 0, \ldots M_x - 1$ and $j = 0, \ldots M_y - 1$, and $M_x = M_y = 512$ in most of the computational results.

We utilize the following discrete Neumann boundary conditions associated with Eqn. (9)

$$c^{n+1}_{x\,-\frac{1}{2},j} = 0, \qquad c^{n+1}_{x\,M_x-\frac{1}{2},j} = 0, \qquad c^{n+1}_{y\,i,-\frac{1}{2}} = 0, \qquad c^{n+1}_{y\,i,M_y-\frac{1}{2}} = 0. \tag{16}$$

Eqn. (16) can be used to set the ghost cell values in x direction as

$$0 = c^{n+1}_{x\,-\frac{1}{2},j} = \left(c^{n+1}_{0,j} - c^{n+1}_{-1,j}\right)/\Delta x \Rightarrow c^{n+1}_{-1,j} = c^{n+1}_{0,j},$$

$$0 = c^{n+1}_{x\,M_x-\frac{1}{2},j} = \left(c^{n+1}_{M_x,j} - c^{n+1}_{M_x-1,j}\right)/\Delta x \Rightarrow c^{n+1}_{M_x,j} = c^{n+1}_{M_x-1,j},$$

and similarly in y direction as

$$0 = c^{n+1}_{y\,i,-\frac{1}{2}} = \left(c^{n+1}_{i,0} - c^{n+1}_{i,-1}\right)/\Delta y \Rightarrow c^{n+1}_{i,-1} = c^{n+1}_{i,0},$$

$$0 = c^{n+1}_{y\,i,M_y-\frac{1}{2}} = \left(c^{n+1}_{i,M_y} - c^{n+1}_{i,M_y-1}\right)/\Delta y \Rightarrow c^{n+1}_{i,M_y} = c^{n+1}_{i,M_y-1}.$$

Here, we note that the discrete equation (13) can be viewed as a system of nonlinear algebraic equations (e.g., $F(c) \approx 0$) to be solved for the unknown c^{n+1}. The resulting nonlinear equation system is solved by using the Jacobian-Free Newton Krylov (JFNK) method Knoll and Keyes (2004); Kadioglu and Knoll (2013); Kadioglu (2017). After performing a specified number of nonlinear iterations, the JFNK method ensures the convergence of all nonlinearities within the system. It is important to note that, like any nonlinear solver, the JFNK method requires a well-chosen initial guess to converge to a physically accurate solution. This requirement is not problematic in this context, as the problem being addressed is an initial value problem. At the start of each time step, an excellent initial guess is naturally provided by the solution from the preceding time step.

3.1 The Jacobian-free Newton Krylov method

In the following section, we briefly describe the JFNK method. The JFNK method has two components namely the Newton and Krylov blocks. The Newton block solves $\mathbf{F}(c) \approx 0$ iteratively over a sequence of linear system defined by

$$\begin{aligned} \mathbf{J}(c^k)\delta c^k &\approx -\mathbf{F}(c^k), \\ c^{k+1} &\approx c^k + \delta c^k, \qquad k = 0, 1, \cdots \end{aligned} \tag{17}$$

where $\mathbf{J}(c^k) = \frac{\partial \mathbf{F}}{\partial c}$ is the Jacobian matrix and δc^k is the update vector. The Newton iteration is stopped, if the following criteria is matched

$$\|\mathbf{F}(c^k)\|_2 < Tol_{res}\|\mathbf{F}(c^0)\|_2, \tag{18}$$

where Tol_{res} is the user defined tolerance (we used 10^{-8} in our calculations). It is important to note that the nonlinear Newton tolerance must be less than the local truncation error to assess the quality of a numerical method. Otherwise, it may become difficult to determine the actual rate of numerical convergence. Generally speaking, if one is not monitoring the pace of convergence, the tolerance does not need to be too strict. Other stopping criteria, such as

$$\left\| F\left(c^k\right)\right\| \leq Tol_{rel}\left\| F\left(c^0\right)\right\| + Tol_{abs}, \tag{19}$$

has been proposed in the literature Singhal et al. (2025) where Tol_{rel} and Tol_{abs} are relative and absolute tolerances, respectively. It is noted in Singhal et al. (2025) that if the magnitude of the initial residual is large (e.g., $\left\| F\left(c^0\right)\right\|$ of $O\left(10^5\right)$), then it may take longer for the nonlinear system to converge to an acceptable tolerance. In such cases, a more conceptual stopping criterion based on the Newton correction term, $\|\delta c\| \leq Tol_c$, is suggested.

The resulting linear system at the Newton correction step (Eqn. 17) is solved by utilizing a Krylov subspace method. In particular, we use the Arnoldi-based GMRES method Saad (2003). A summary of the algorithmic steps of the GMRES method is provided in Sect. 3.2. At the beginning of the GMRES iteration, we define an initial residual, $\mathbf{r}_0$, for a given initial guess δc_0,

$$\mathbf{r}_0 \approx -\mathbf{F}(c) - \mathbf{J}\delta c_0. \tag{20}$$

Since the Krylov (GMRES) iteration is executed at a fixed k, we omit the index k for convenience in Eqn. (20). Let j denote the Krylov iteration index. The j^{th} Krylov iteration minimizes the quantity $\|\mathbf{J}\delta c_j + \mathbf{F}(c)\|_2$ within a subspace of small dimension, relative to n (the number of unknown vectors), in a least-squares sense. δc_j is drawn from the subspace spanned by the Krylov vectors, $\{\mathbf{r}_0, \mathbf{J}\mathbf{r}_0, \mathbf{J}^2\mathbf{r}_0, \cdots, \mathbf{J}^{j-1}\mathbf{r}_0\}$, and can be written as the following combination

$$\delta c_j \approx \delta c_0 + \sum_{i=0}^{j-1} \beta_i (\mathbf{J})^i \mathbf{r}_0, \tag{21}$$

where the term β_i minimizes the residual. We terminate the Krylov iteration using the following inexact Newton criteria Dembo et al. (1982)

$$\|J\delta c_j + \mathbf{F}(c)\|_2 < \gamma\|\mathbf{F}(c)\|_2. \tag{22}$$

Here, the parameter γ is chosen to determine the convergence of the linear solver at each Newton iteration (we usually set $\gamma = 10^{-3}$). We note that one main advantage of the Krylov subspace method that we use here is that it does not need the formation of the Jacobian matrix.

It only requires the matrix–vector multiplication, $\mathbf{Jv}$, where $\mathbf{v} \in \{\mathbf{r}_0, \mathbf{Jr}_0, \mathbf{J}^2\mathbf{r}_0, \cdots\}$. This is why it is simply referred to as the *Jacobian-Free* implementation in which the operation of the Jacobian matrix times a vector can be estimated by

$$\mathbf{Jv} \approx \frac{\mathbf{F}(c + \epsilon\mathbf{v}) - \mathbf{F}(c)}{\epsilon}, \tag{23}$$

where $\epsilon = \frac{1}{n\|\mathbf{v}\|_2} \sum_{i=1}^{n} b|c_i| + b$, n is the dimension of the linear system, and b is a constant whose magnitude is within a few orders of magnitude of the square root of machine round-off (it is typically set to 10^{-6} for 64-bit double precision).

As previously mentioned, we employ a preconditioning technique to accelerate the convergence of the Krylov step in the Jacobian-Free Newton-Krylov (JFNK) method. Typically, when a preconditioner is applied, the original linear system (17) is modified by multiplying the Jacobian matrix by a preconditioning matrix, either from the left or right. If the multiplication occurs from the left, the resulting method is referred to as a left preconditioner, while multiplication from the right defines a right preconditioner. It is important to note that the left preconditioner also modifies the right-hand side of the linear system (17), requiring the recovery of the modified nonlinear residuals. This introduces additional complexities in terms of both coding and computational cost Knoll and Keyes (2004); Saad (2003); Brown and Saad (1990). In contrast, the right preconditioner does not alter the right-hand side term and does not present the associated difficulties. For this reason, we adopt the right preconditioning (RP) strategy in this study. The RP procedure modifies the linear system (17) in the following way

$$\mathbf{J}P^{-1}(P\delta c) \approx -\mathbf{F}(c), \tag{24}$$

where P is the preconditioning matrix. The action of the right preconditioning can be defined similar to (23), e.g.,

$$\mathbf{J}P^{-1}\mathbf{v} \approx \frac{\mathbf{F}(c + \epsilon P^{-1}\mathbf{v}) - \mathbf{F}(c)}{\epsilon}, \tag{25}$$

where $\mathbf{v}$ is the Krylov vector. The execution of this procedure involves the following steps:

$$\begin{aligned} &\textbf{Step-1:} \text{ Given } \mathbf{v}, \text{ solve } Pz = \mathbf{v} \text{ for } z \ (e.g., z = P^{-1}\mathbf{v}) \\ &\textbf{Step-2:} \text{ Perform } \mathbf{J}z \approx (\mathbf{F}(c + \epsilon z) - \mathbf{F}(c))/\epsilon, \end{aligned} \tag{26}$$

where z is the preconditioned Krylov vector. In Section 3.3, we describe a methodology for obtaining $z's$.

3.2 Basic structure of the preconditioned flexible GMRES algorithm

We refer this algorithm as the flexible GMRES method because at each iteration the preconditioning matrix can change (as it does in our description, Sect. 3.3) rather than using one fix matrix for all iterations.

1. Compute $r_0 = -\mathbf{F}(c) - \mathbf{J}\delta c_0$ from (20) and $\beta = \|r_0\|_2$, $v_1 = r_0/\beta$
2. For $j = 1, \ldots, m$
3. Compute $z_j = P_j^{-1} v_j$ (equivalently solve $P_j z_j = v_j$ for z_j, Preconditioning step)
4. Compute $w_j = Jz_j$ applying (23), Jacobian-Free step
5. For $i = 1, \ldots, j$
6. Compute $h_{i,j} = (w_j, v_i)$
7. Compute $w_j = w_j - h_{i,j} v_i$

8. End
9. Compute $h_{j+1,j} = \|w_j\|_2$, if $h_{j+1,j} \approx 0$ set $m = j$ go to **11**
10. Compute $v_{j+1} = w_j / h_{j+1,j}$
11. Define $Z_m = [z_1, \cdots, z_m]$, $\bar{H}_m = \{h_{i,j}\}_{1 \le i \le m+1, 1 \le j \le m}$
12. End
13. Compute $y_m = argmin_y \|\beta e_1 - \bar{H}_m y\|_2$
14. Set $\delta c_m = \delta c_0 + Z_m y_m$
15. If converged, (22) is satisfied, stop. Otherwise set $\delta c_0 = \delta c_m$ go to **1**, restart GMRES

3.3 The physics-based preconditioner

The preconditioning approach utilized in this work is the partial differential equation (PDE)-based method, also referred to as the physics-based approach Kelley (2003); Knoll and Keyes (2004); Zhang et al. (2019). Different classes of PDEs are associated with distinct physical processes. For example, hyperbolic PDEs characterize wave phenomena, whereas parabolic PDEs describe diffusion processes. Certain physical systems, such as fluid flow, may exhibit both parabolic and hyperbolic characteristics. Importantly, various physical processes may operate on different time scales, resulting in governing equations with varying degrees of stiffness. The stiffness of the system influences the choice of numerical techniques, with explicit methods typically suited for non-stiff problems, implicit methods for stiff systems, and semi-implicit methods for systems with mixed characteristics. Stiff components in the equations often impose stringent time-step restrictions. Thus, incorporating physical insights into the model allows for the identification and targeted treatment of specific stiff terms–diffusion terms in this case–enabling larger time steps and facilitating faster convergence of the underlying linear algebra problem (in this case, the Krylov subspace problem).

Matrix-based preconditioning techniques, such as LU decomposition, incomplete LU (ILU) and its variants, and other related approaches Saad (2003); Scott and Tuma (2023), are well-established methods for accelerating the convergence of linear systems. However, a significant limitation of these methods is their reliance on some information about the Jacobian matrix of the nonlinear system. As previously noted, constructing the Jacobian matrix can be computationally challenging, and its storage is often resource intensive. In contrast, our matrix-free approach, based on the Jacobian-Free Newton-Krylov (JFNK) method, eliminates the need for explicit Jacobian formation or storage. Similarly, our preferred physics-based preconditioner also avoids the explicit construction of both the preconditioning matrix and its inverse. Instead, it computes the action of the inverse preconditioning matrix on a Krylov vector. This simple structure enables straightforward and flexible code implementation. The reliability and efficiency of this preconditioning approach are thoroughly evaluated and discussed in the Results section.

We follow the steps of Kadioglu and Knoll (2013); Kadioglu (2017); Kadioglu and Ozugurlu (2023) to derive the preconditioning equation. First, we recast the discretization (13) as

$$\frac{c_{i,j}^{k+1} - c_{i,j}^{n}}{\Delta t} - \frac{[(Dc_x)_x]_{i,j}^{k+1} + [(Dc_x)_x]_{i,j}^{n}}{2} - \frac{[(Dc_y)_y]_{i,j}^{k+1} + [(Dc_y)_y]_{i,j}^{n}}{2} \approx \frac{f_{i,j}^{k} + f_{i,j}^{n}}{2}, \tag{27}$$

where

$$f_{i,j}^{n} = \rho c_{i,j}^{n} \left(1 - \frac{c_{i,j}^{n}}{\kappa}\right) - R_{i,j}^{n} c_{i,j}^{n} \left(1 - \frac{c_{i,j}^{n}}{\kappa}\right) - G_{i,j}^{n}. \tag{28}$$

Adding and subtracting $c_{i,j}^k$ to the time part and adding $[(Dc_x)_x]_{i,j}^k/2$, $[(Dc_y)_y]_{i,j}^k/2$ to both sides of Eqn. (27) and assuming $\delta c_{i,j} = c_{i,j}^{k+1} - c_{i,j}^k$, we obtain

$$\frac{\delta c_{i,j}}{\Delta t} - \frac{[(Dc_x)_x]_{i,j}^{k+1} - [(Dc_x)_x]_{i,j}^k}{2} - \frac{[(Dc_y)_y]_{i,j}^{k+1} - [(Dc_y)_y]_{i,j}^k}{2} \approx -\left(\frac{c_{i,j}^k - c_{i,j}^n}{\Delta t} - \frac{[(Dc_x)_x]_{i,j}^k + [(Dc_x)_x]_{i,j}^n}{2} - \frac{[(Dc_y)_y]_{i,j}^k + [(Dc_y)_y]_{i,j}^n}{2} - \frac{f_{i,j}^k + f_{i,j}^n}{2}\right). \tag{29}$$

If we let

$$\mathrm{resc}_{i,j}^k \approx c_{i,j}^k - c_{i,j}^n - \frac{\Delta t}{2}\left([(Dc_x)_x]_{i,j}^k + [(Dc_x)_x]_{i,j}^n + [(Dc_y)_y]_{i,j}^k + [(Dc_y)_y]_{i,j}^n + f_{i,j}^k + f_{i,j}^n\right),$$

and assume that the diffusion coefficient, D, is approximately the same at k and $k+1$ nonlinear iterations and make use of the discretizations (14) and (15) together with $\delta c_{i,j} = c_{i,j}^{k+1} - c_{i,j}^k$, then Eqn.(29) becomes,

$$\delta c_{i,j} - \frac{\Delta t}{2\Delta x^2} D_{i+\frac{1}{2},j}(\delta c_{i+1,j} - \delta c_{i,j}) + \frac{\Delta t}{2\Delta x^2} D_{i-\frac{1}{2},j}(\delta c_{i,j} - \delta c_{i-1,j}) - \frac{\Delta t}{2\Delta y^2} D_{i,j+\frac{1}{2}}(\delta c_{i,j+1} - \delta c_{i,j}) + \frac{\Delta t}{2\Delta y^2} D_{i,j-\frac{1}{2}}(\delta c_{i,j} - \delta c_{i,j-1}) \approx -\mathrm{resc}_{i,j}^k. \tag{30}$$

Equation (30) can be rewritten as

$$-c\delta c_{i-1,j} - b\delta c_{i+1,j} + a\delta c_{i,j} - d\delta c_{i,j+1} - e\delta c_{i,j-1} \approx -\mathrm{resc}_{i,j}^k, \tag{31}$$

where

$$a = 1 + \frac{\Delta t}{2\Delta x^2} D_{i+\frac{1}{2},j} + \frac{\Delta t}{2\Delta x^2} D_{i-\frac{1}{2},j} + \frac{\Delta t}{2\Delta y^2} D_{i,j+\frac{1}{2}} + \frac{\Delta t}{2\Delta y^2} D_{i,j-\frac{1}{2}},$$
$$b = \frac{\Delta t}{2\Delta x^2} D_{i+\frac{1}{2},j}, \quad c = \frac{\Delta t}{2\Delta x^2} D_{i-\frac{1}{2},j}, \quad d = \frac{\Delta t}{2\Delta y^2} D_{i,j+\frac{1}{2}}, \quad e = \frac{\Delta t}{2\Delta y^2} D_{i,j-\frac{1}{2}}, \tag{32}$$

for $i = 1, ..., M_x - 1$ and $j = 1, ..., M_y - 1$. Here $\mathrm{resc}_{i,j}^k$ represents the nonlinear residual term at the k^{th} iteration.

Notice that we need boundary conditions when solving Eqn. (31) for δc. Essentially we define few ghost cell values as $\delta c_{-1,j} \approx \delta c_{0,j}$ and $\delta c_{M_x,j} \approx \delta c_{M_x-1,j}$ for $j = 1, ..., M_y - 1$ and $\delta c_{i,-1} \approx \delta c_{i,0}$ and $\delta c_{i,M_y} \approx \delta c_{i,M_y-1}$ for $i = 1, ..., M_x - 1$. The update equation (31) is solved iteratively to produce the preconditioned Krylov vector $z = \delta c$ defined in Eqn. (26).

The iterative procedure employs a multi-grid V-cycle method tailored specifically for our applications. A typical multi-grid V-cycle method involves a sequence of recursively applied Gauss-Seidel (GS) iterations or other basic smoothers, such as Jacobi iterations, progressing from the finest grid level to the coarsest and back to the finest Briggs (2000); Kelley (2003). It is well established that GS and similar iterative methods are highly effective in damping high-frequency errors within just a few iterations. However, these methods are notoriously slow in achieving fully converged solutions, with the required iteration count often scaling with problem size (e.g., $M_x \times M_y$ in our 2D cases), rendering them impractical for large problems. To address this, we leverage the GS smoother in designing our multi-grid V-cycle. At the start of each V-cycle, *two* GS iterations are performed on the finest grid to attenuate high-frequency errors. The solution is then restricted to a coarser grid, where coarse solutions and residuals are computed, followed by *two* additional GS sweeps. At this coarser

Table 1 R_{eff} values for different α choices in Conventional and Hyperfractioned radiotherapy models

	Conventional Radiotherapy			Hyperfractioned Radiotherapy					
	$Dose = 2\,Gy$			$Dose = 2 \times 1.2\,Gy$			$Dose = 2 \times 1.3\,Gy$		
$\alpha\ (1/Gy)$	0.018	0.027	0.036	0.018	0.027	0.036	0.018	0.027	0.036
R_{eff}	0.0432	0.0648	0.0864	0.0639	0.0958	0.1278	0.0711	0.1066	0.1422

level, previously low-frequency errors manifest as high-frequency errors, allowing them to be smoothed effectively with a small number of GS iterations. This process is recursively repeated down to the coarsest grid level, which consists of *two* cells in each direction. At this level, *hundred* GS iterations are performed to ensure thorough smoothing. Following the coarsest level computations, a prolongation step is applied recursively to interpolate the coarse solutions back to finer grid levels. On each finer level, *two* additional GS sweeps are conducted. This sequence of steps constitutes a single multi-grid V-cycle. In our test cases, we found that *five* V-cycles were sufficient to significantly reduce the GMRES iteration count. However, the number of multi-grid V-cycles can be adjusted as needed, depending on the specifics of the physical model and its numerical discretization.

4 Numerical results

In the subsequent subsections, we present the results of our numerical experiments, which investigate both conventional and hyperfractionated radiotherapy treatments in conjunction with simultaneously and adjuvantly administered chemotherapy. Table 1 provides a summary of the radiotherapy parameters and the corresponding effective radiotherapy coefficients utilized in the governing eqns. (4) and (35).

4.1 Conventional concurrent radio-chemo therapy treatment

Initially, we provide the mathematical framework underlying the conventional radio-chemotherapy treatment strategy. Specifically, we detail the radiotherapy and chemotherapy parameters, along with the associated temporal functions utilized in Eqns. (5) and (8). This treatment regimen assumes that concurrent radio-chemotherapy begins at $t = 180$ days, corresponding to the point at which the tumor radius becomes detectable. The combined radio-chemo therapy is administered over a six-week period. Radiotherapy is delivered at a daily dose rate of $2\,Gy$ per fraction over *five* days per week (excluding weekends), culminating in a total dose of $60\,Gy$ (Fig. 4). This radiotherapy targets gross tumor volumes within a radius of $2 - 3\,cm$, including an additional safety margin Powathil et al. (2007). Concurrently, chemotherapy employs temozolomide administered daily at a dose of $75\,mg/m^2$ (or $0.0075\,mg/cm^2$) throughout the week. The resulting chemotherapy-induced cell death rate is $k = 0.00735\,day^{-1}$, as represented in Equation (7), and this dosage persists for the entire duration of radiotherapy Powathil et al. (2007); Agosti et al. (2017). Following the six-week concurrent treatment, patients undergo up to six cycles of adjuvant chemotherapy. Each cycle involves *five* days of chemotherapy administration per week, separated by a 28-day interval. The initial cycle, commencing at the *eleventh* week, begins with a dosage of $150\,mg/m^2$ (or $0.015\,mg/cm^2$), corresponding to a chemotherapy-induced death rate of $k = 0.0147\,day^{-1}$.

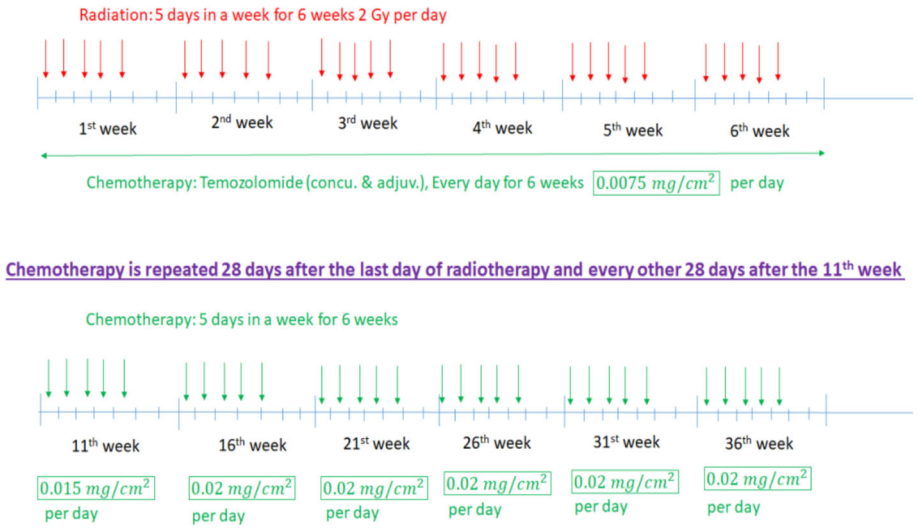

Fig. 4 The clinical and model schedule for combination of radiotherapy and (concurrent and adjuvant) chemotherapy

Subsequently, the dosage is increased to $200\,mg/m^2$ (or $0.02\,mg/cm^2$), with an associated death rate of $k = 0.0196\,day^{-1}$ (refer to Fig. 4). Based on these treatment scenarios, the temporal functions in Eqns. (5) and (8), activated at $t = 180$ days, are refined as

$$R_{timer}(n_{week}, d_{day}) = \begin{cases} 1 \text{ if } n_{week} \leq 6 \text{ and } d_{day} \leq 5 \\ 0 \text{ otherwise .} \end{cases} \tag{33}$$

$$C_{timer}(n_{week}, d_{day}) = \begin{cases} 1 \text{ if } n_{week} \leq 6 \text{ and } d_{day} \leq 7 \\ 1 \text{ if } n_{week} \leq 11 \text{ and } d_{day} \leq 5 \\ 1 \text{ if } n_{week} \leq 16 \text{ and } d_{day} \leq 5 \\ 1 \text{ if } n_{week} \leq 21 \text{ and } d_{day} \leq 5 \\ 1 \text{ if } n_{week} \leq 26 \text{ and } d_{day} \leq 5 \\ 1 \text{ if } n_{week} \leq 31 \text{ and } d_{day} \leq 5 \\ 1 \text{ if } n_{week} \leq 36 \text{ and } d_{day} \leq 5 \\ 0 \text{ otherwise .} \end{cases} \tag{34}$$

For comparative analysis, simulations also consider scenarios without treatment, allowing the tumor to proliferate uninterrupted. The left panel of Fig. 5 depicts the normalized total number of tumor cells, while the right panel illustrates the simulated tumor area up to the critical radius associated with mortality (~ 3 cm). The mathematical details of the computation of these quantities are presented in Sect. 2. The model predicts that in the absence of therapy, the tumor size reaches the critical radius around 54 weeks, consistent with clinical observations Powathil et al. (2007); Samadifam and Ghafourian (2023). Figure 5 demonstrates that the initiation of simultaneous radio-chemotherapy significantly reduces the tumor cell count and the corresponding detectable tumor area during the six-week treatment. Following this period, chemotherapy alone continues per the schedule in Fig. 4. Notably, the right panel of Fig. 5 indicates that survival time increases by approximately 12 weeks when comparing the minimum and maximum values of $\alpha's$. Furthermore, a comparison of the maximum α value

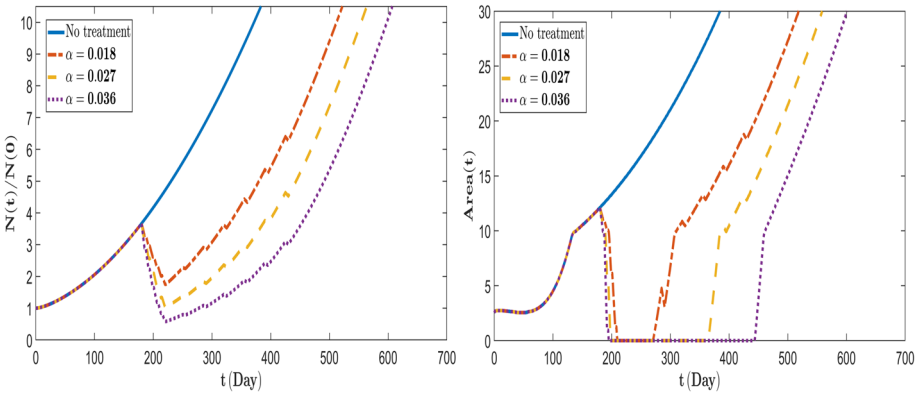

Fig. 5 The conventional radio-chemo therapy starts at $t = 180\,days$ with $Dose = 2\,Gy$. Left: the normalized total number of tumor cells, Right: the simulated tumor area up to the critical radius

with the untreated case reveals a survival extension of approximately 28 weeks, highlighting the efficacy of the combined treatment approach.

4.2 Hyperfractioned concurrent radio-chemo therapy treatment

The hyperfractionated radiotherapy is proposed based on the clinical findings that some patients can be highly sensitive to the single administration (conventional) of high-dosage irradiation Powathil et al. (2007); Samadifam and Ghafourian (2023). In other words, single-dose irradiation can be toxic and cause damage to healthy tissues, particularly in older individuals Samadifam and Ghafourian (2023). To reduce the toxicity and minimize harm to the healthy tissues surrounding malignant tumors, the dosage is frequently administered in two fractions daily. In a typical hyperfractionated concurrent radio-chemotherapy treatment, a dose of 1.2 Gy or 1.3 Gy is delivered twice daily with a six-hour interval, five days per week, over a total of six weeks (Fig. 4). Fractions ranging from 1.5 Gy to 1.8 Gy have also been reported in the literature Powathil et al. (2007); Samadifam and Ghafourian (2023); Nieder et al. (1999). The concurrent chemotherapy associated with hyperfractionated radiotherapy, as well as the subsequent adjuvant chemotherapy, follows the same drug dosage parameters and temporal scheduling functions as described in Sect. 4.1. It is noteworthy that the irradiation duration is standardized at 12 min for both conventional and hyperfractionated radiotherapy Samadifam and Ghafourian (2023). The hyperfractionated radio-chemotherapy treatment employs the same governing eqns. (1) - (11) as the conventional approach, except that the effective radiotherapy term in Equation (4) is modified as

$$R_{eff} = 2\,\alpha\, Dose(x,t)\left[1 + \frac{Dose(x,t)}{\alpha/\beta}\left(1 + e^{-\mu(\tau+\Delta\tau)}\right)\right], \tag{35}$$

where τ denotes the irradiation duration, $\Delta\tau$ is the time interval between fractions, and μ represents the repair half rate. The derivation of (35) and other equivalency formulas are presented in the Appendix. The parameters in (35), with appropriate units, are $\tau = 12\,min = 8.3 \times 10^{-3}\,day$, $\mu = 0.46\,h^{-1} = 1.9 \times 10^{-2}\,day^{-1}$, $\Delta\tau = 0.25\,day$ and therefore $\mu\tau \approx 1.5 \times 10^{-4}$, $\mu\Delta\tau \approx 4.7 \times 10^{-3}$.

Figure 6 illustrates the results of administering two daily fractions with a dose of 1.2 Gy per fraction, under varying values of α. The corresponding effective radiotherapy function

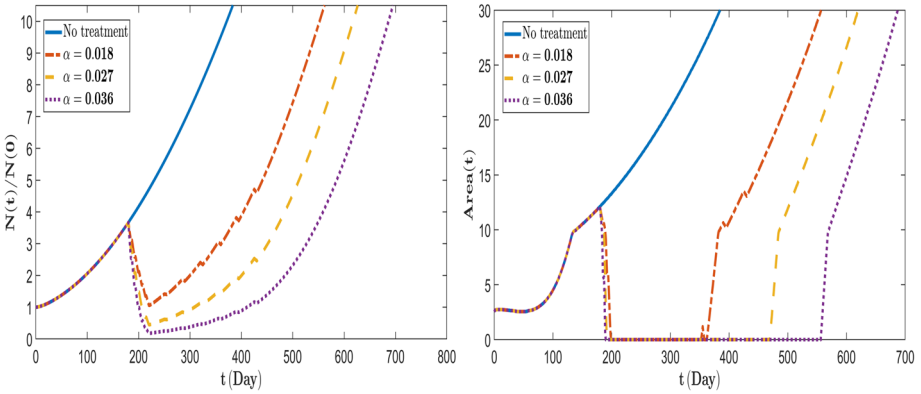

Fig. 6 The hyperfractioned radio-chemo therapy starts at $t = 180\,days$ with $Dose = 1.2\,Gy$. Left: the normalized total number of tumor cells, Right: the simulated tumor area up to the critical radius

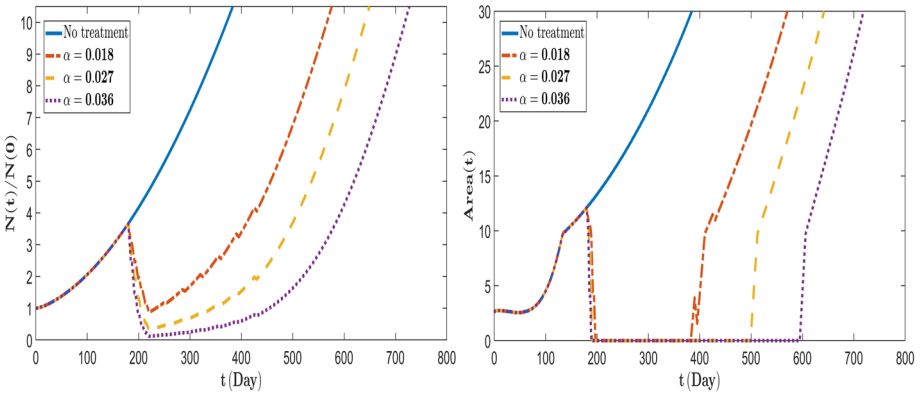

Fig. 7 The hyperfractioned radio-chemo therapy starts at $t = 180\,days$ with $Dose = 1.3\,Gy$. Left: the normalized total number of tumor cells, Right: the simulated tumor area up to the critical radius

values are listed in Table 1. Compared to conventional treatment, hyperfractionated therapy yields significant improvements in patient outcomes. For instance, for $\alpha = 0.036$, survival time extends to 42 weeks, compared to 28 weeks with conventional therapy. The most notable improvement occurs with hyperfractionated treatment at a dose of 1.3 Gy per fraction, delivered twice daily. As shown in Fig. 7, survival time is extended to approximately 48 weeks for $\alpha = 0.036$.

4.3 Numerical accuracy and efficiency analysis

The theoretical order of accuracy of our numerical scheme is *second-order* in space and time. Theoretical convergence orders are well-established for linear models and linear numerical schemes. However, when dealing with nonlinear models or solutions exhibiting sharp structures, verifying the expected order of accuracy becomes challenging. Both these complexities are present in our model and its solution profiles. Consequently, it is essential to assess whether numerical accuracy is preserved in our computations. While analytical solutions to the Fisher-Kolmogorov equation exist for specific situations and could be used for

Table 2 Numerical convergence analysis with $M_x = M_y = 1024$, $\Delta t = 10^{-1}$

Time convergence analysis with $E = \|\|c^{\Delta t/2^{k-1}} - c^{\Delta t/2^k}\|\|_p$ in columns 1,3,5					
$p = 1$ $k = 1, ..., 8$	Conv. rate r in (36)	$p = 2$ $k = 1, ..., 8$	Conv. rate r in (36)	$p = \infty$ $k = 1, ..., 8$	Conv. rate r in (36)
2.92×10^{-2}	2.00	4.29×10^{-2}	2.00	1.71×10^{-1}	2.00
7.30×10^{-3}	2.00	1.07×10^{-2}	2.00	4.27×10^{-2}	2.00
1.82×10^{-3}	2.00	2.67×10^{-3}	2.00	1.06×10^{-2}	2.00
4.56×10^{-4}	2.00	6.69×10^{-4}	2.00	2.67×10^{-3}	1.99
1.14×10^{-4}	2.00	1.67×10^{-4}	2.00	6.67×10^{-4}	2.00
2.85×10^{-5}	1.97	4.18×10^{-5}	1.95	1.66×10^{-4}	1.94
7.25×10^{-6}	2.10	1.08×10^{-5}	1.98	4.34×10^{-5}	2.05
1.68×10^{-6}		2.74×10^{-6}		1.04×10^{-5}	

comparison, we opt for computational approaches to conduct the convergence analysis. This preference arises from the flexibility of numerical analysis, which can be readily extended to more general problems, such as coupled nonlinear fluid dynamics systems incorporating additional physical effects. The convergence analysis follows a systematic procedure. We fix the spatial resolution, e.g., $M_x = M_y = 1024$, and perform computations with progressively refined time steps up to a final time $t_{final} = 10$. The approximate solution set, $c^{\Delta t}, c^{\frac{\Delta t}{2}}, c^{\frac{\Delta t}{4}}, \ldots, c^{\frac{\Delta t}{2^k}}$, is obtained for $k = 0, 1, \ldots, 8$ and $\Delta t = 10^{-1}$. We then compute the L_p-norms of the errors between consecutive time-step solutions, for $p \in \{1, 2, \infty\}$,

$$||c^{\Delta t} - c^{\frac{\Delta t}{2}}||_p, \ ||c^{\frac{\Delta t}{2}} - c^{\frac{\Delta t}{4}}||_p, \ldots$$

These error values can be plotted on a log scale alongside reference second-order slope indicators to visualize convergence behavior. Alternatively, the convergence rate can be quantified directly by

$$r = \ln\left(||E(\Delta t/2^{k-1})||/||E(\Delta t/2^k)||\right) / \ln 2, \tag{36}$$

where

$$E(\Delta t/2^{k-1}) = ||c^{\Delta t/2^{k-1}} - c^{\Delta t/2^k}||_p \qquad k = 1, \ldots, 8.$$

To validate the numerical scheme, we constructed a convergence table (Table 2) to verify its theoretical second-order accuracy. The convergence rates, while slightly varying with the choice of norm, consistently approach the theoretical value of *two*. This validation is critical as it demonstrates the reliability of our code implementation and numerically confirms that the Jacobian-Free Newton-Krylov (JFNK) method preserves the theoretical order of accuracy and consistently converges all nonlinearities in the physical system as intended.

Additionally, we conducted an efficiency study to evaluate the effectiveness of the numerical scheme when equipped with a preconditioner. For this purpose, we ran the simulation with $\Delta t = 1$ and $M_x = M_y = 512$, and a final time $t_{final} = 45.0$, both with and without the preconditioner. Figure 8 illustrates the significant reduction in the number of nonlinear (Newton block) and linear (Krylov block) iterations when the preconditioner is employed. Specifically, the average number of Krylov iterations genuinely decreased from approximately 50 to 12, while the average number of Newton iterations halved from 18 to 9. This

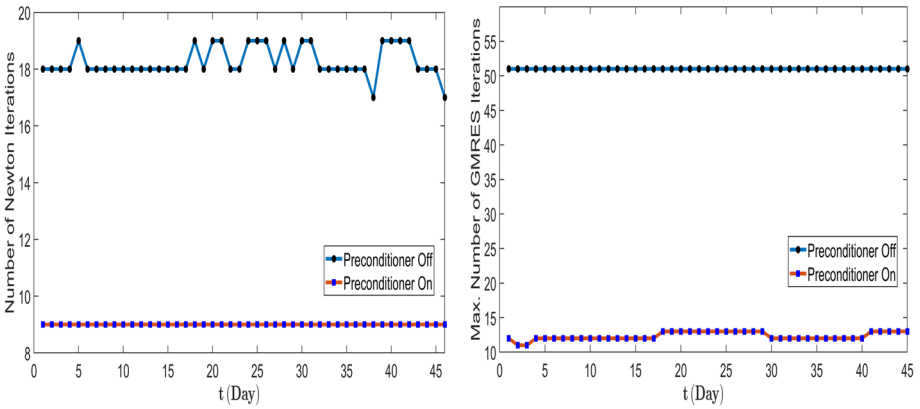

Fig. 8 Efficiency study of the numerical method with and without the preconditioner

notable improvement in numerical efficiency is important when extending the approach to three-dimensional and more complex tumor models.

Building upon the observed improvements in numerical efficiency, we compare the performance of the proposed method with some of the state of the art methods such as ILU preconditioners. Incomplete Lower-Upper (ILU) factorizations are very efficient preconditioning techniques for approximately inverting the true or approximate Jacobian matrix during the preconditioning step. ILU methods compute a sparse matrix factorization by selectively excluding matrix elements that are either too small or fall outside a predefined sparsity pattern, thereby controlling the amount of fill-in introduced during factorization. The ILU(k) factorization allows fill-in up to level k, where the level indicates the maximum number of fill-in steps permitted beyond the original sparsity pattern. In the case of ILU(0), the factorization preserves the original sparsity pattern with zero fill-in, meaning no additional non-zero elements are introduced during factorization. By carefully optimizing the fill-in levels, the ILU(k) methods can offer a robust approach that approximates the exact LU decomposition of the Jacobian matrix Saad (2003); Scott and Tuma (2023). The following comparative study employs the same computational settings as those used to produce Fig. 8. In all preconditioner options, the identical nonlinear equation is solved under consistent convergence criteria. Since a preconditioner influences only the efficiency and not the solution itself, the overall numerical accuracy remains intact. The findings, presented in Table 3, display the average number of Newton and Krylov iterations alongside the corresponding CPU times. Regarding the ILU methods, ILU(0) lowers the computational cost per iteration due to its sparser structure, but typically demands more iterations, which can lead to increased total computation time. Conversely, the ILU(1) and ILU(2) preconditioners successfully reduce both the number of Newton and Krylov iterations and the overall CPU time. The physics-based multigrid (PB-MG) preconditioner delivers the best overall performance by minimizing iteration counts and total CPU time. Without any preconditioning, the solver demands substantially more iterations and incurs the highest computational cost.

Table 3 Preconditioners performance study with 512×512 grid and $\Delta t = 1.0$ at $t_{final} = 45.0$

Preconditioners	Newton iterations	Krylov iterations	CPU time / Krylov (s)	CPU time / Δt (s)	Total CPU Time (s)
NONE	18	52	0.0036	3.4	153.0
ILU(0)	14	38	0.0038	2.05	92.3
ILU(1)	12	26	0.0054	1.68	75.6
ILU(2)	10	19	0.0064	1.21	54.5
PB-MG	9	12	0.0080	0.87	39.2

5 Conclusions

Brain glioma, particularly glioblastoma multiform (GBM), remains a significant challenge in medical science due to its complex and invasive nature. Despite advancements in surgical, radio-therapeutic, and chemotherapeutic interventions, GBM often exhibits resistance to these treatments, necessitating innovative strategies. This study highlights the promising role of mathematical and computational modeling in understanding and optimizing treatment approaches for gliomas. By simulating the interactions between radiotherapy, chemotherapy, and tumor progression using sophisticated models, such as those employing the Jacobian-free Newton Krylov (JFNK) method with advanced preconditioning techniques, we can enhance computational efficiency and accuracy and therefore treatment efficacy. The numerical results emphasize the potential of these models to optimize treatment strategies, ultimately aiming to improve patient outcomes. In line with clinical observations, our computational model predicts that the tumor size will reach the lethal radius around 54 weeks if treatment is not received. The numerical simulations further reveal that combined administration of radiotherapy and chemotherapy markedly reduces both tumor cell populations and the associated detectable tumor area. The computational results also suggest that the hyperfractionated therapy significantly improves patient outcomes as compared to traditional treatment. Regarding the computational aspects, we confirmed theoretical second-order accuracy through a numerical convergence study, validating the reliability of our code and providing evidence that the JFNK method consistently converges all nonlinearities in the physical system as anticipated. Moreover, an efficiency analysis comparing our novel preconditioning approach with established techniques such as ILU methods showed that the new preconditioner outperforms in terms of reducing nonlinear and linear iterations and lowering CPU time.

Ongoing advancements in computational resources and algorithmic design will be essential for translating these theoretical models into practical clinical tools. Future work should focus on further refining these models to support more personalized and effective treatment plans, enabling simulations of more realistic tumor sizes and complex treatment dynamics, thereby offering hope for improved management and outcomes for patients suffering from this devastating disease.

6 Appendix

The conventional or hyperfractioned radiotherapy treatment is commonly modeled by the following effective radio therapy function Powathil et al. (2007); Ghafourian et al. (2023)

$$R_{eff} = n\,\alpha\, Dose + n\,\beta\, Dose^2 \left[g(\mu\tau) + 2\left(\frac{\cosh(\mu\tau)-1}{(\mu\tau)^2}\right) h_n(\varphi)\right], \tag{37}$$

where $n = 1$ means the conventional and $n \geq 2$ corresponds to the hyperfractioned therapy. The other radio-biological coefficients are described in Sect. 2. The functions involved in (37) are defined as

$$\varphi = e^{-\mu(\tau+\Delta\tau)}, \tag{38}$$

$$g(\mu\tau) = 2\,\frac{\mu\tau - 1 + e^{-\mu\tau}}{(\mu\tau)^2}, \tag{39}$$

$$h_n(\varphi) = 2\,\frac{n\varphi - n\varphi^2 - \varphi + \varphi^{n+1}}{n(1-\varphi)^2}. \tag{40}$$

For the conventional radio therapy case, $n = 1$, we have $h_1(\varphi) = 0$ and

$$R_{eff} = \alpha\, Dose + \beta\, Dose^2\, g(\mu\tau). \tag{41}$$

Using the following Taylor series in function $g(\mu\tau)$, we get

$$e^{-\mu\tau} = 1 - \mu\tau + \frac{(\mu\tau)^2}{2} - \frac{(\mu\tau)^3}{6} + \frac{(\mu\tau)^4}{24} + \cdots$$

$$\begin{aligned} g(\mu\tau) &= 2\,\frac{\mu\tau - 1 + \left(1 - \mu\tau + \frac{(\mu\tau)^2}{2} - \frac{(\mu\tau)^3}{6} + \frac{(\mu\tau)^4}{24} + \cdots\right)}{(\mu\tau)^2} \\ &= 1 - \frac{\mu\tau}{3} + \frac{(\mu\tau)^2}{12} + \cdots \end{aligned} \tag{42}$$

Considering the typical values for the irradiation duration, $\tau = 12\,min = 8.3 \times 10^{-3}\,day$, the repair half rate $\mu = 0.46\,h^{-1} = 1.9 \times 10^{-2}\,day^{-1}$, and $\mu\tau \approx 1.5 \times 10^{-4}$, the value of function g gets close to *one* (e.g., $g(\mu\tau) \approx 0.99995 \approx 1.0$). With this, Eqn. (41) becomes

$$R_{eff} \approx \alpha\, Dose + \beta\, Dose^2. \tag{43}$$

After utilizing an appropriate Taylor series for the exponential term, it can be easily shown that our model Eqn. (4) is equivalent to Eqn. (43).

Now, for the hyperfractioned radio therapy case, $n = 2$ (assuming daily *two* fractions), we have

$$R_{eff} = 2\,\alpha\, Dose + 2\,\beta\, Dose^2 \left[g(\mu\tau) + 2\left(\frac{\cosh(\mu\tau)-1}{(\mu\tau)^2}\right) h_2(\varphi)\right], \tag{44}$$

where

$$h_2(\varphi) = 2\,\frac{2\,\varphi - 2\,\varphi^2 - \varphi + \varphi^3}{2\,(1-\varphi)^2} = \varphi. \tag{45}$$

Applying an appropriate Taylor series expansion, the hyperbolic term becomes

$$\left(\frac{\cosh(\mu\tau)-1}{(\mu\tau)^2}\right)=\frac{1}{2}+\frac{(\mu\tau)^2}{24}+\frac{(\mu\tau)^4}{720}+\cdots \tag{46}$$

which is approximately $1/2$ since $(\mu\tau)^2/24 \approx 9.3\times 10^{-10}$. Using these and recalling $g(\mu\tau)\approx 0.99995\approx 1.0$, and substituting (38) in (44), we obtain

$$R_{eff}\approx 2\,\alpha\,Dose+2\,\beta\,Dose^2\left[1.0+e^{-\mu(\tau+\Delta\tau)}\right], \tag{47}$$

which can be simplified as

$$R_{eff}\approx 2\,\alpha\,Dose\left[1+\frac{Dose}{\alpha/\beta}\left(1+e^{-\mu(\tau+\Delta\tau)}\right)\right]. \tag{48}$$

Data availability Not applicable.

Declarations

Conflict of interest We have no conflict of interest to disclose.

References

Agosti A, Antonietti PF, Ciarletta P, Grasselli M, Verani M (2017) A Cahn-Hilliard type equation with application to tumour growth dynamics. Math Methods Appl Sci 40:7598–7626

Ansarizadeh F, Singh M, Richards D (2017) Modelling of tumor cells regression in response to chemotherapeutic treatment. Appl Math Model 48:96–112

Athanassiou H, Synodinou M, Maragoudakis E, Paraskevaidis M, Verigos C, Misailidou D, Antonadou D, Saris G, Beroukas K, Karageorgis P (2005) Randomized phase ii study of temozolomide and radiotherapy compared with radiotherapy alone in newly diagnosed glioblastoma multiforme. J Clin Oncol 723:2372–2377

Barani IJ, Larson DA (2015) Radiation therapy of glioblastoma. Cancer Treat Res 163:49–73

Barazzuol L, Burnet NG, Jena R, Jones B, Jefferies SJ, Kirkby NF (2010) A mathematical model of brain tumors response to radiotherapy and chemotherapy considering radiobiological aspects. J Theor Biol 262:553–565

Bashkirtseva I, Chukhareva A, Ryashko L (2021) Modeling and analysis of nonlinear tumor-immune interaction under chemotherapy and radiotherapy. Math Methods Appl Sci 45:7983–7991

Briggs WL (2000) A Multigrid Tutorial., SIAM

Brown P, Saad Y (1990) Hybrid krylov methods for nonlinear systems of equations. SIAM J Sci Stat Comput 11:450–481

Damm KA, Gibbons NN, Jacobs PA, Gollan R (2023) Application of a jacobian-free newton-krylov method to the simulation of hypersonic flows, in Aiaa Scitech 2023 Forum, p. 2295

Dehghan M, Narimani N (2018) An element-free Galerkin meshless method for simulating the behavior of cancer cell invasion of surrounding tissue. Appl Math Model 59:500–513

Damm K, Gibbons N, Jacobs P, Gollan R (2020) Radial basis function-generated finite difference scheme for simulating the brain cancer growth model under radiotherapy in various types of computational domains. Comput Methods Programs Biomed 195:105641

Deisboeck TS (2009) Personalizing medicine: a systems biology perspective. Mol Syst Biol 5(1):249

Dembo R, Eisenstat SC, Steihaug T (1982) Inexact newton methods. SIAM J Num Anal 19:400–408

Elazab A, Anter AM, Bai H, Hu Q, Hussain Z, Ni D, Wang T, Lei B (2019) An optimized generic cerebral tumor growth modeling framework by coupling biomechanical and diffusive models with treatment effects. Appl Soft Comput 80:617–627

Ghafourian E, Samadifam F, Fadavian H, Canatalay PJ, Tajally A, Channumsin S (2023) An ensemble model for the diagnosis of brain tumors through mris. Diagnostics 13:561

Hathout L, Ellingson B, Pope W (2016) Modeling the efficacy of the extent of surgical resection in the setting of radiation therapy for glioblastoma. Cancer Sci 107:1110–1116

Hormuth-II DA, Farhat M, Christenson C, Curl B, Quarles C, Chung C et al (2022) Opportunities for improving brain cancer treatment outcomes through imaging-based mathematical modeling of the delivery of radiotherapy and immunotherapy. Adv Drug Delivery Rev 187:114367
Kadioglu S (2017) A second-order imex method for multi-phase flow problems. Int J Comput Methods 14–5:1750056
Kadioglu S, Knoll D, Sussman M, Martineau R (2011) A second order JFNK-based IMEX method for single and multi-phase flows, Comput Fluid Dyn, Springer, pp. 549–554
Kadioglu SY (2017) Analysis of the self-consistent imex method for tightly coupled non-linear systems. J Comput Appl Math 322:148–160
Kadioglu SY, Knoll DA (2013) A Jacobian-Free Newton Krylov implicit-explicit time integration method for incompressible flow problems. Commun Comput Phys 13–5:1408–1431
Kadioglu SY, Ozugurlu E (2023) A Jacobian-Free Newton-Krylov method to solve tumor growth problems with effective preconditioning strategies. Appl Sci 13(11):6579
Kapoor M, Joshi V (2021) Numerical approximation of 1d and 2d reaction diffusion system with modified cubic uah tension b-spline dqm. J Math Comput Sci 11:1650–1667
Kelley CT (2003) Solving Nonlinear Equations with Newton's Method., Siam
Khan I, Baig MH, Mahfooz S, Imran MA, Khan MI, Dong JJ, Cho JY, Hatiboglu MA (2022) Nanomedicine for glioblastoma: progress and future prospects. Semin Cancer Biol 86:172–186
Khayrullaev H, Omle I, Kovács E (2025) Exploring the performance of some efficient explicit numerical methods with good stability properties for Huxley's equation. Mathematics 13:207
Knoll DA, Keyes DE (2004) Jacobian-Free Newton–Krylov methods: a survey of approaches and applications. J Comput Phys 193:357–397
Kothari H, Kopanicáková A, Krause R (2023) A multigrid preconditioner for jacobian-free newton-krylov methods, in Domain decomposition methods in science and engineering XXVI, Springer, pp. 365–372
Kovács E, Majar J, Saleh M (2024) Unconditionally positive, explicit, fourth order method for the diffusion-and Nagumo-type diffusion-reaction equations. J Sci Comput 98:39
Kuznetsov M, Kolobov A (2023) Optimization of antitumor radiotherapy fractionation via mathematical modeling with account of 4r's of radiobiology. J Theor Biol 558:111371
LeVeque R (1998) Finite Volume Methods for Hyperbolic Problems., Cambridge University Press , Texts in Applied Mathematics
Liu P, Liu X (2017) Dynamics of a tumor-immune model considering targeted chemotherapy. Chaos Solit Fractals 98:7–13
Mach J, Benes M, Strachota P (2017) Nonlinear Galerkin finite element method applied to the system of reaction-diffusion equations in one space dimension. Comput Math Appl 73:2053–2065
Mihalef V, Kadioglu S, Sussman M, Metaxas D, Hurmusiadis V (2008) Interaction of two-phase flow with animated models. Graph Models 70–3:33–42
Moreau G, Francois-Lavet V, Desbordes P, Macq B (2021) Reinforcement learning for radiotherapy dose fractioning automation. Biomedicines 9:214
Moshtaghi-Kashanian N, Niroomand-Oscuii H, Meghdadi N (2018) Simulating glioblastoma growth consisting both visible and invisible parts of the tumor using a diffusion-reaction model followed by resection and radiotherapy. Acta Neurol Belg 120:629–637
Nieder C, Nestle U, Niewald M, Walker K, Schnabel K (1999) Hyperfractioned reirradiation for malignant glioma. Front Radiat Ther Oncol 33:150–7
Park H, Gaston D, Kadioglu S, Knoll D (2009) Tightly coupled multiphysics simulations for pebble bed reactors.,
Parney IF, Chang SM (2003) Current chemotherapy for glioblastoma. Cancer J 9:149–156
Perry RH (2012) The chemotherapy source book. Wolters Kluwer Health, Lippincott Williams and Wilkins, Philadelphia
Plaszczynski S, Grammaticos B, Pallud J, Campagne JE, Badoual M (2023) Predicting regrowth of low-grade gliomas after radiotherapy. PLoS Comput Biol 19(3):e1011002
Powathil G, Adamson D, Chaplain M (2013) Towards predicting the response of a solid tumour to chemotherapy and radiotherapy treatments: clinical insights from a computational model. PLoS Comput Biol 9:e1003120
Powathil G, Kohandel M, Sivaloganathan S, Oza A, Milosevic M (2007) Mathematical modeling of brain tumors: effects of radiotherapy and chemotherapy. Phys Med Biol 52:3291
Powathil GG, Swat M, Chaplain MAJ (2015) Systems oncology: towards patientspecific treatment regimes informed by multiscale mathematical modelling. Semin Cancer Biol 30:13–20
Rockne R, Alvord E, Rockhill J, Swanson KR (2009) A mathematical model for brain tumor response to radiation therapy. J Math Biol 58:561–578

Rockne R, Rockhill JK, Mrugala M, Spence AM, Kalet I, Lai KHA, Cloughesy T, Alvord EC, Swanson KR (2010) Predicting the efficacy of radiotherapy in individual glioblastoma patients in vivo: a mathematical modeling approach. Phys Med Biol 55:3271–85

Roniotis A, Marias K, Sakkalis V, Zervakis M (2010) Diffusive modelling of glioma evolution: a review. J Biomed Sci Eng 3:501–508

Saad Y (2003) Iterative methods for sparse linear systems, SIAM

Samadifam F, Ghafourian E (2023) Mathematical modeling of the treatment response of resection plus combined chemotherapy and different types of radiation therapy in a glioblastoma patient. arXiv:2308.07976

Schuetz TA, Mang A, Becker S, Toma A, Buzug TM (2014) Identification of crucial parameters in a mathematical multiscale model of glioblastoma growth, Comput Math Methods, pp. 1–14

Scott J, Tuma M (2023) Algorithms for sparse linear systems, Springer Nature

Shim E, Kwon Y, Ko H (2005) Computational analysis of tumor angiogenesis patterns using a two-dimensional model., Yonsei. Med J 46:275–283

Singhal R, Dogrul EC, Bai Z (2025) Jacobian-free newton-krylov with a globalization method for solving groundwater flow models of multi-layer aquifer systems. arXiv:2505.08884

Stupp R, Hegi ME, Mason WP, van den Bent MJ, Taphoorn MJB, Janzer RC, Ludwin SK, Allgeier A, Fisher B, Belanger K, Hau P, Brandes AA, Gijtenbeek J, Marosi C, Vecht CJ, Mokhtari K, Wesseling P, Villa S, Eisenhauer E, Gorlia T, Weller M, Lacombe D, Cairncross JG, Mirimanoff RO (2009) Effects of radiotherapy with concomitant and adjuvant temozolomide versus radiotherapy alone on survival in glioblastoma in a randomised phase iii study: 5-year analysis of the eortc-ncic trial. Lancet Oncol 10:459–466

Stupp R, Mason WP, van den Bent MJ, Weller M, Fisher B, Taphoorn MJB, Belanger K, Brandes AA, Marosi C, Bogdahn U, Curschmann J, Janzer RC, Ludwin SK, Gorlia T, Allgeier A, Lacombe D, Cairncross JG, Eisenhauer E, Mirimanoff RO (2005) N Eng J 352:987–996

Swanson KR, Alvord EC, Murray JD (2002) Quantifying efficacy of chemotherapy of brain tumors (gliomas) with homogeneous and heterogeneous drug delivery. Acta Biotheor 50:223–237

Swanson KR, Bridge C, Murray JD, Alvord EC (2003) Virtual and real brain tumors: using mathematical modeling to quantify glioma growth and invasion. J Neurol Sci 216:1–10

Swanson KR, Harpold HLP, Peacock DL, Rockne R, Pennington C, Kilbride L, Grant R, Wardlaw JM, Alvord EC (2008) Velocity of radial expansion of contrast-enhancing gliomas and the effectiveness of radiotherapy in individual patients: a proof of principle. Clin Oncol 20:301–308

Thomas J (1998) Numerical partial differential equations I (finite difference methods)., Springer-Verlag New York, Texts in Applied Mathematics

Tracqui P, Cruywagen GC, Woodward DE, Bartoo GT, Murray JD, Alvord EC (1995) A mathematical model of glioma growth: the effect of chemotherapy on Spatio-temporal growth. Cell Prolif 28:17–31

Tseng TYCYY, Liu SJ (2021) Role of polymeric local drug delivery in multimodal treatment of malignant glioma: a review. Int J Nanomed 16:4597–4614

Usher JR, Abercrombie DA (1981) Case studies in cancer and its treatment by radiotherapy. Int J Math Educ Sci Technol 12:661–682

Walker MD, Alexander E, Hunt WE, Leventhal CM, Mahaley MS, Mealey J, Norrell HA, Owens G, Ransohoff J, Wilson CB, Gehan EA (1976) Evaluation of mithramycin in the treatment of anaplastic gliomas. J Neurosurg 44:655–667

Walker MD, Green SB, Byar DP, Alexander E, Batzdorf U, Brooks WH, Hunt WE, MacCarty CS, Mahaley MS, Mealey J, Owens G, Ransohoff J, Robertson JT, Shapiro WR, Smith KR, Wilson CB, Strike TA (1980) Randomized comparisons of radiotherapy and nitrosoureas for the treatment of malignant glioma after surgery. N Engl J 303(71980):1323–1329

Wang C, Rockhill J, Mrugala M, Peacock D, Lai A, Jusenius K et al (2009) Prognostic significance of growth kinetics in newly diagnosed glioblastomas revealed by combining serial imaging with a novel biomathematical model. Cancer Res 69:9133–40

Woodward DE, Cook J, Tracqui P, Cruywagen GC, Murray JD, Alvord EC (1996) A mathematical model of glioma growth: the effect of extent of surgical resection. Cell Prolif 29:269–288

Wu G, Lee EWM, Li G (2015) Numerical solutions of the reaction-diffusion equation: an integral equation method using the variational iteration method. Int J Numer Methods Heat Fluid Flow 25:265–271

Zade AE, Haghighi S, Soltani M (2022) Deep neural networks for neuro-oncology: towards patient individualized design of chemo-radiation therapy for glioblastoma patients. J Inf 127:104006

Zhang H, Guo J, Lu J, Li F, Xu Y (2019) The comparison between nonlinear and linear preconditioning JFNK method for transient neutronic/thermal-hydraulics coupling problem. Ann Nucl Energy 132:357–368

Zhao J, Wei X, Tian J (2022) Modeling of tumor radiotherapy with damage and repair processes. Eur Phys J Plus 137(5):584